Article

Tailoring Magnetic Properties of $Fe_{0.65}Co_{0.35}$ Nanoparticles by Compositing with RE_2O_3 (RE = La, Nd, and Sm)

Nacira Djellal [1], Paweł Pęczkowski [2,*], Djamel Eddine Mekki [3], Elena Navarro [4,5], Tarek Tahraoui [1,6], Jarosław Piętosa [7], Jan Marek Michalik [8], Pilar Marín [4,5] and Łukasz Gondek [8]

1   Mines Metallurgy Materials Laboratory L3M, Department of Materials Science and Engineering, National Higher School of Mining and Metallurgy, Annaba 23000, Algeria
2   Institute of Physical Sciences, Faculty of Mathematics and Natural Sciences, School of Exact Sciences, Cardinal Stefan Wyszyński University, K. Wóycickiego 1/3 Street, 01-938 Warsaw, Poland
3   LESIMS, Department of Physics, Faculty of Science, University of Badji Mokhtar, Annaba 23000, Algeria
4   Instituto de Magnetismo Aplicado, Universidad Complutense de Madrid (UCM-ADIF), 28230 Las Rozas, Spain
5   Departamento de Física de Materiales, Universidad Complutense de Madrid (UCM), 28040 Madrid, Spain
6   National Higher School of Technology and Engineering—ENSTI, Sidi Amar, Annaba 23000, Algeria
7   Group of Phase Transition, Division of Physics of Magnetism, Institute of Physics, Polish Academy of Sciences, Lotników 32/46 Avenue, 02-668 Warsaw, Poland
8   Department of Solid State Physics, Faculty of Physics and Applied Computer Science, AGH University of Science and Technology, A. Mickiewicza 30 Avenue, 30-059 Kraków, Poland
*   Correspondence: p.peczkowski@wp.pl or p.peczkowski@uksw.edu.pl

Abstract: Fe-Co alloys are the most important soft magnetic materials, which are successfully used for a wide range of applications. In this work, the magnetic properties of lanthanide-substituted $(Fe_{0.65}Co_{0.35})_{0.95}(RE_2O_3)_{0.05}$ (RE = La, Nd, and Sm) nanoparticles, prepared by mechanical alloying, are reported. Our comprehensive studies (X-ray diffraction, Mössbauer spectroscopy, scanning electron microscopy with X-ray energy dispersive spectrometry, SQUID magnetometry and differential scanning calorimetry) have revealed different properties, depending on the dopant type. The RE_2O_3 addition led to a decrease in the crystallite size and to an increase in the internal microstrain. Moreover, because of the high grain fragmentation tendency of RE_2O_3, the cold welding between Fe–Co ductile particles was minimized, indicating a significant decrease in the average particle size. The parent $Fe_{0.65}Co_{0.35}$ alloy is known for its soft ferromagnetism. For the La-substituted sample, the magnetic energy product was significantly lower (0.450 MG·Oe) than for the parent alloy (0.608 MG·Oe), and much higher for the Sm-substituted compound (0.710 MG·Oe). The processing route presented here, seems to be cost-effective for the large-scale production of soft magnetic materials.

Keywords: Fe–Co; $Fe_{0.65}Co_{0.35}$; nanoparticles; rare-earth elements; soft magnetic materials

1. Introduction

Soft magnetic nanoparticles (SMNs) represent an important field in materials science and engineering, since they exhibit unique and interesting characteristics that provide promising applications [1]. Typically, SMNs include ferrites, Fe–Ni, Fe–Si, Fe–Al, and Fe–Co based alloys, which have been studied intensively in recent years [1–19]. Fe–Co nanoparticles show high saturation magnetization and Curie temperature values, allowing the development of numerous applications, such as hyperthermia magnetic treatment [2] or thermoablative cancer therapy [3], magnetic resonance imaging (MRI) contrast [4,5] (currently the most commonly used gadolinium diethylenetriaminepentaacetic acid - Gd–DTPA [6]), high-density data storage [1,7], advanced materials for microwave devices [8], exchange-spring permanent magnets [1,9], and new generation of magnetorheological

fluids [10]. Until now, it is generally known that the $Fe_{0.65}Co_{0.35}$ alloy has the highest saturation magnetization value. In order to obtain better magnetic properties, several substitutions on $Fe_{0.65}Co_{0.35}$, by various elements, have been undertaken, including Cr [11,12], Si [13,14], Si and Co [14] , Ni [15], Al [16], Cu [17], V [18], and Dy [19].

Another interesting observation is the combination of complementary features of Fe–Co ($3d$ - itinerant magnetism) with rare-earth metals ($4f$ – localized). The $4f$ rare-earth metals exhibit a strong magnetic susceptibility and high magnetocrystalline anisotropy, due to the interactions between their orbital moment and the crystalline field. Alloying them with a $3d$ metal induces their polarization, and therefore consolidates the magnetization of the alloy [20,21]. The rare-earth metals exhibit large ionic radii, which can modify the cell symmetry, and therefore generate internal stress, while substituting atoms with smaller ionic radii in the structure. Therefore, the structural, magnetic and magnetostrictive properties (e.g., cell parameter, average crystallite, and grain sizes) of the alloy are modified [21]. Studies on transition metal rare-earth (T-R) compounds show a fundamental interest in magnetic coupling and development of interface walls. Unfortunately, studies on T-R alloys are limited by the cost of rare-earth elements and their low oxidation stability. Interestingly, the Fe–Co system was not subjected, to the best of our knowledge, to compositing with rare-earth oxides. The motivation behind such research was the much lower cost of oxides when compared to pure elemental lanthanides.

In this work, we present the effects of RE_2O_3 (RE = La, Nd, and Sm) substitution on the structural, microstructural, morphological and magnetic behavior of mechanically alloyed $Fe_{0.65}Co_{0.35}$ nanoparticles. The mechanically alloyed $Fe_{0.65}Co_{0.35}$ compound exhibits the highest saturation magnetization within the Fe–Co family, and is well known for its soft magnetic properties [22,23].

2. Materials and Methods

2.1. Synthesis and Preparation of Samples

Initial Fe (Alfa Aesar, 99%, d < 10 µm), Co (Alfa Aesar, 99.8%, 1.6 µm), La_2O_3 (Alfa Aesar, 99.9%), Nd_2O_3 (Alfa Aesar, 99.9%), and Sm_2O_3 (Alfa Aesar, 99.9%) powders were used to prepare the $Fe_{0.65}Co_{0.35}$ alloy and the corresponding $(Fe_{0.65}Co_{0.35})_{0.95}(RE_2O_3)_{0.05}$ (RE = La, Nd, and Sm) samples with effective high-energy ball milling. It was found that 1% of impurity of Fe powder was caused mostly by oxygen (Fe_3O_4). The initial powders were mechanically alloyed (MA), in the appropriately prepared amounts, using a vibrating ball mill Retsch MM 400 with two cylindrical vials (25 mL, WC) and balls (10 mm, WC). The frequency of milling was kept at 20 Hz for 3 h, because for these mechanosynthesis parameters, the best structural and magnetic properties of the samples were obtained [22–24]. The ball to powder ratio was maintained at 25:1; around 50% of the vial volume was empty to assure suitable space for the milling process. In order to prevent excessive heating of the powders, the MA was stopped 15 min after every 15 min of milling.

2.2. Research Methods

The morphology and chemical composition of the samples were investigated with a JEOL-6100 scanning electron microscope (SEM), equipped with an X-ray energy dispersive spectrometer (EDS). The average particle size was estimated by scanning electron micrographs using ImageJ software.

The analyses of the structural properties were performed using the X-ray diffraction (XRD) method in an X'Pert MPD diffractometer. The anticathode of copper with $\lambda_{K\alpha1}$ = 0.15406 nm was employed to obtain diffraction spectra. The range of 2θ was 5–100°, with a scanning step of 0.02°, and an exposure time of one second per step. The refined crystallite size, lattice parameter and microstrain were obtained using MAUD (Materials Analysis Using Diffraction) software.

In addition, ^{57}Fe Mössbauer measurements were carried out at room temperature, in the transmission mode, utilizing a constant acceleration spectrometer with ^{57}Co in a

rhodium matrix as the source. The obtained spectra were fitted using the Gauss–Newton's iterative method of minimizing the χ^2, with a Lorentzian shape of the spectral lines.

The measurements of the dependence of magnetization *M* as a function of the magnetic field *H* (*M-H* - hysteresis loops) were carried out using a superconducting quantum interference device (SQUID) magnetometer produced by Quantum Design GmbH in the applied magnetic field up to 50 kOe.

Structural phase transformations and magnetic ordering temperature were determined by differential scanning calorimetry (DSC), using DSC 404 NETZSCH. The measurements in the temperature range from 25 °C to 1200 °C were performed under protective nitrogen gas, with a heating rate of 30 °C/min.

3. Results and Discussion

3.1. Scanning Electron Microscopy (SEM) Analysis

The morphology, particle size and chemical composition of pure and *RE*-substituted $Fe_{0.65}Co_{0.35}$ nanoparticles were investigated by SEM. Figure 1 shows the scanning electron microscopy (SEM) images of the local microstructures of the following samples: $(Fe_{0.65}Co_{0.35})_{0.95}(La_2O_3)_{0.05}$ (**a**), $(Fe_{0.65}Co_{0.35})_{0.95}(Nd_2O_3)_{0.05}$ (**b**), $(Fe_{0.65}Co_{0.35})_{0.95}(Sm_2O_3)_{0.05}$ (**c**), and $Fe_{0.65}Co_{0.35}$ (3 h) (**d**).
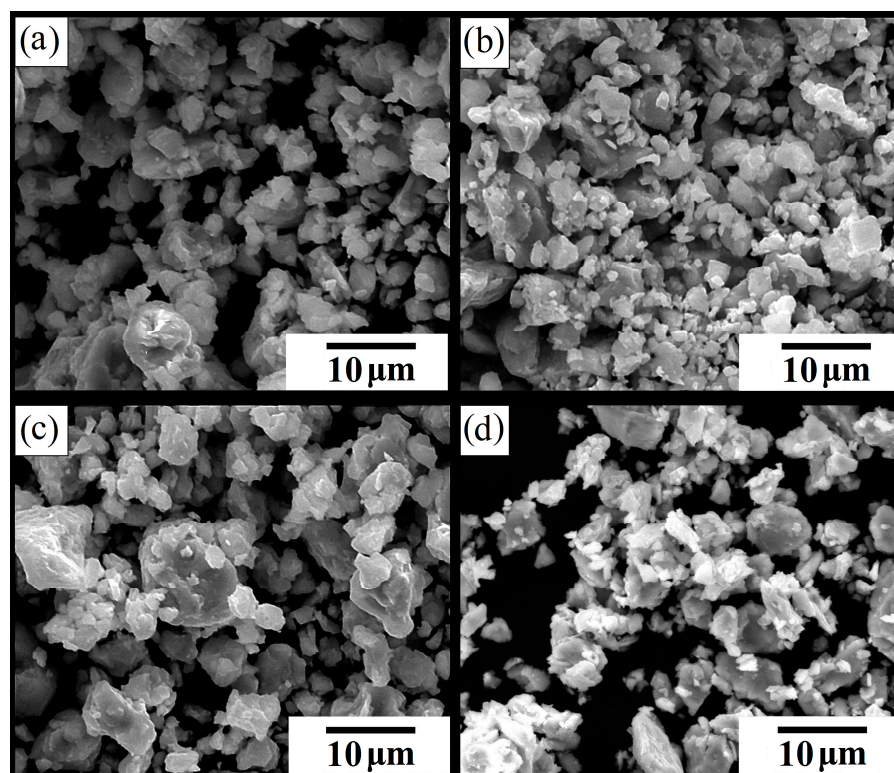

Figure 1. Scanning electron microscopy (SEM) images of the local microstructures of the following samples: (**a**) $(Fe_{0.65}Co_{0.35})_{0.95}(La_2O_3)_{0.05}$, (**b**) $(Fe_{0.65}Co_{0.35})_{0.95}(Nd_2O_3)_{0.05}$, (**c**) $(Fe_{0.65}Co_{0.35})_{0.95}(Sm_2O_3)_{0.05}$, and (**d**) $Fe_{0.65}Co_{0.35}$ (3 h).

It can be observed that the particles of pure and *RE*-substituted $Fe_{0.65}Co_{0.35}$ (3 h) samples have an irregular shape. A large number of agglomerates and clusters was noticed. This was explained by the presence of strong magnetic interactions in the Fe–Co based alloys and by the high surface energy in the grain boundaries of powders produced during effective high-energy ball milling [25]. The average particle size distribution of all compositions is presented in Figure 2.
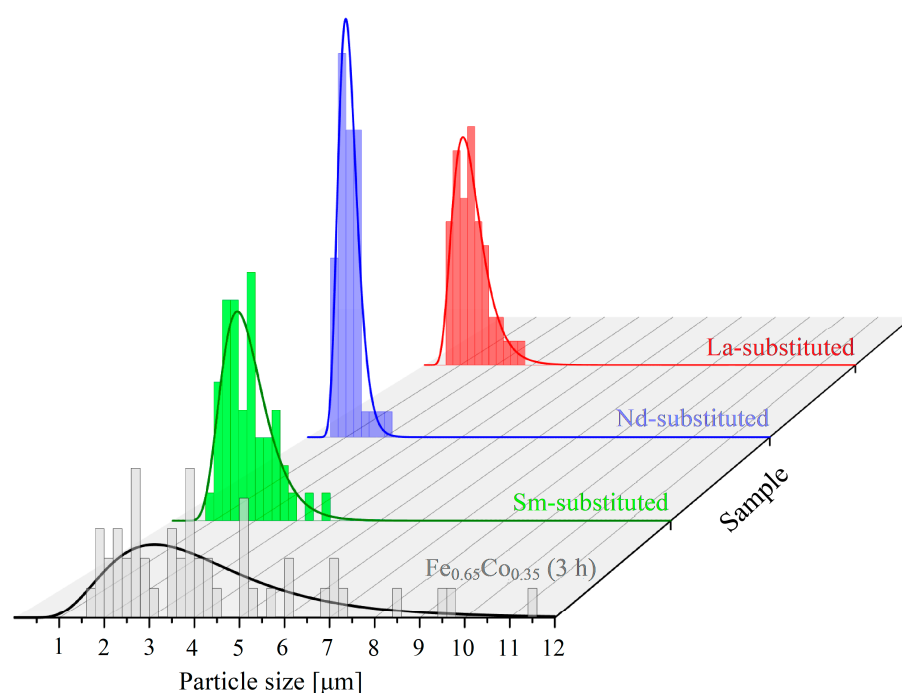
Figure 2. Average particle size distribution of $Fe_{0.65}Co_{0.35}$ and $(Fe_{0.65}Co_{0.35})_{0.95}(RE_2O_3)_{0.05}$ (RE = La, Nd, and Sm) formed during effective high-energy ball milling for 3 h.

It can be observed that the average particle size distribution of RE-substituted samples is smaller than that for the pure $Fe_{0.65}Co_{0.35}$ (3 h) sample. This was explained by the increase in the hardness and brittleness of Fe-Co ductile powders after RE_2O_3 substitution [25].

The addition of RE_2O_3 leads to an increase in the grain fragmentation of Fe-Co powders, and to a decrease in the particle size. The decrement in the particle size after the RE-substitution can also be explained by the presence of secondary phases ($NdFeO_3$ and $LaFeO_3$) located at the grain boundaries, which can hinder the particles' growth [26].

EDS analysis revealed elemental abundances, which are summarized in Table 1. It is thought that the samples show the appropriate stoichiometry. The short duration of high-energy milling prevented contamination from the milling vial and balls (tungsten carbide).

Table 1. Results of X-ray microprobe analysis (EDS) recorded for the obtained powders.

Samples	Fe [at%]	Co [at%]	RE [at%]
$Fe_{0.65}Co_{0.35}$ (3 h)	65.2(1)	34.8(1)	-
$Fe_{0.65}Co_{0.35} - 5$ wt% La_2O_3 (La-substituted sample)	64.3(1)	34.6(1)	1.1(1)
$Fe_{0.65}Co_{0.35} - 5$ wt% Nd_2O_3 (Nd-substituted sample)	64.9(1)	34.0(1)	1.1(1)
$Fe_{0.65}Co_{0.35} - 5$ wt% Sm_2O_3 (Sm-substituted sample)	64.4(1)	33.9(1)	1.2(1)

Figure 3 shows the chemical distribution of the $(Fe_{0.65}Co_{0.35})_{0.95}(La_2O_3)_{0.05}$ sample. All constituents are homogenously dispersed in ferrite particles after 3 h of milling. This indicates that the elements are completely incorporated into the Fe structure. No traces of grains of RE_2O_3 oxides were detected.
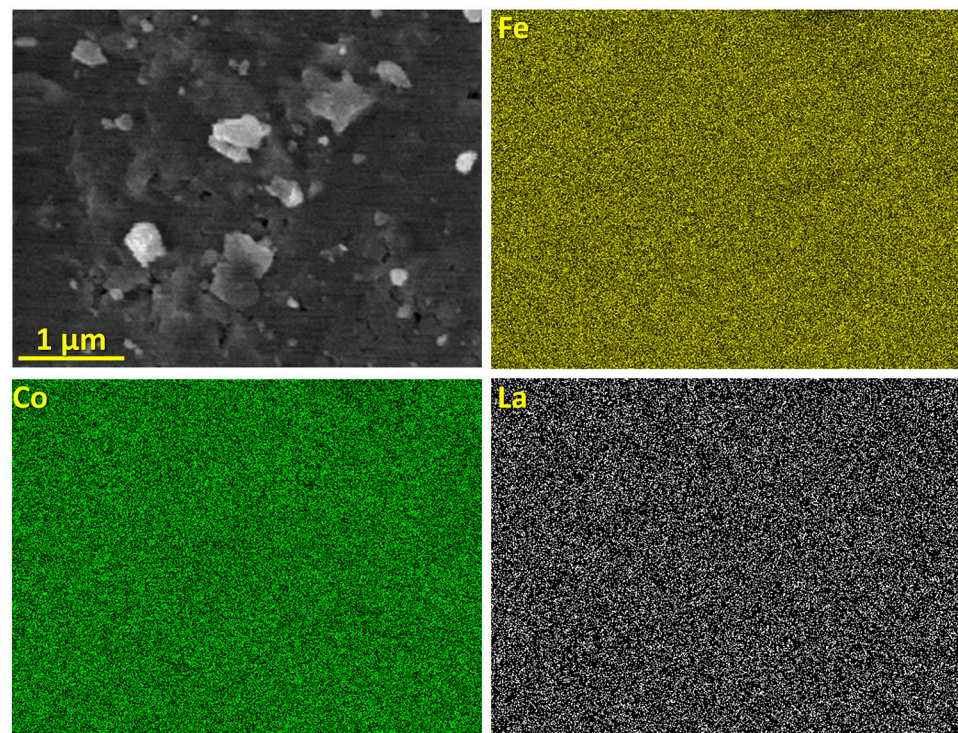
Figure 3. Chemical distribution of $(Fe_{0.65}Co_{0.35})_{0.95}(La_2O_3)_{0.05}$ sample.

3.2. X-ray Diffraction (XRD) Analysis

The structural and microstructural properties of the lanthanide-substituted $Fe_{0.65}Co_{0.35}$ (3 h) nanoparticles were investigated using the X-ray diffraction (XRD) technique. The XRD patterns of the prepared nanoparticles are shown in Figure 4.
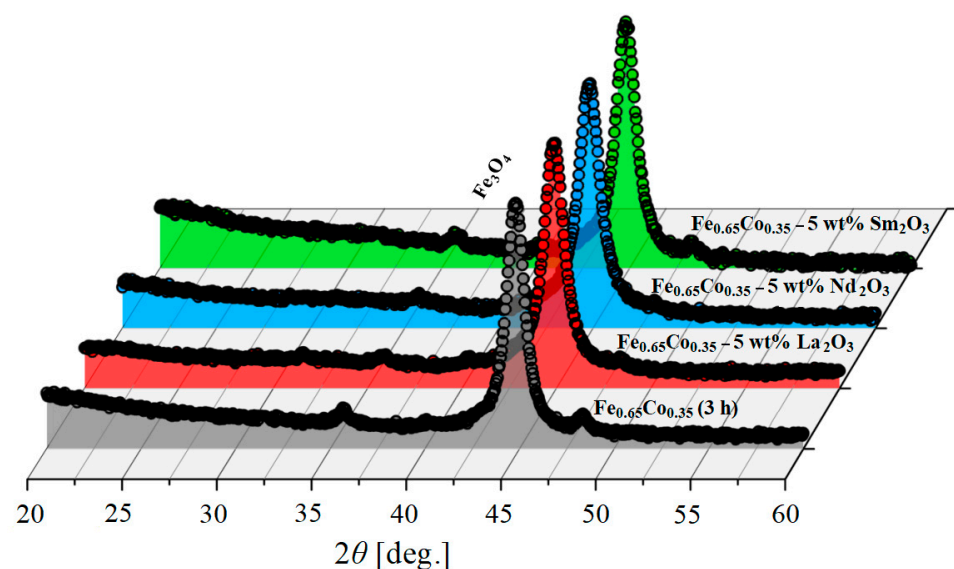

Figure 4. X-ray diffraction (XRD) patterns of $Fe_{0.65}Co_{0.35}$ (3 h) alloy and $(Fe_{0.65}Co_{0.35})_{0.95}(RE_2O_3)_{0.05}$ samples with RE = La, Nd, and Sm. The Y-axis was square-rooted to magnify small peaks.

Figure 4 shows the XRD spectrums of the $Fe_{0.65}Co_{0.35}$ (3 h) alloy and $(Fe_{0.65}Co_{0.35})_{0.95}(RE_2O_3)_{0.05}$ samples with RE = La, Nd, and Sm. The characteristic peaks of Co, La_2O_3, Nd_2O_3, and Sm_2O_3 are no longer visible after 3 h of milling. The XRD patterns show the peaks characteristic for the body-centered cubic (bcc) iron structure ($Im3m$, COD 04-004-2474) for all

investigated samples. These results confirm that Co, La^{3+}, Nd^{3+}, Sm^{3+}, and O^{2-} were dissolved in the bcc-Fe structure. Traces of Fe_3O_4 are observed for all investigated specimens due to the initial impurity of Fe powder. Furthermore, extremely small peaks seem to originate from traces of the REFeO$_3$ phase, as presented by Suo et al. [27] and Kanna et al. [28]. The presence of these secondary phases suggests that the solubility of La^{3+} and Nd^{3+} inside the bcc-Fe structure is not complete due to their large radius (1.15 Å and 0.983 Å, respectively) [27]. However, the Sm^{3+} ions with a smaller radius are completely incorporated into the $Fe_{0.65}Co_{0.35}$ nanoparticles, as no additional peaks of any impurity phase were detected (Figure 4). The difference between the Fe and Co atomic radii is less than 15% and they also have the same valence (+3), which is necessary to reach a maximum solubility between atoms [29]. Moreover, the electro-negativity values of Fe and Co are almost the same, 1.83 and 1.88, respectively, which leads to a high solubility between them according to the Hume-Rothery rules [30,31]. The crystallite size, microstrain and lattice parameter refined by the Rietveld analysis, for the $Fe_{0.65}Co_{0.35}$ alloy and $(Fe_{0.65}Co_{0.35})_{0.95}(RE_2O_3)_{0.05}$ samples with RE = La, Nd, and Sm, are shown in the Figure 5. The lattice parameters are the same for all the samples within the experimental error.

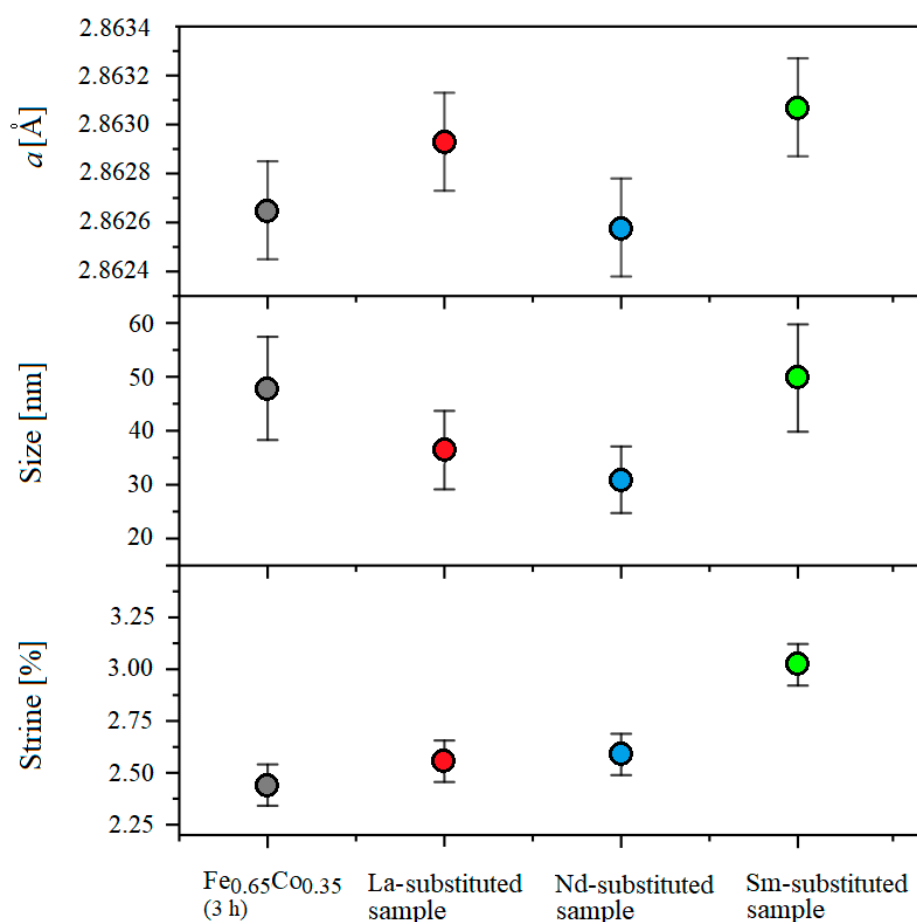**Figure 5.** The crystallite size, microstrain and lattice parameter refined by the Rietveld analysis for pure $Fe_{0.65}Co_{0.35}$ alloy and for $(Fe_{0.65}Co_{0.35})_{0.95}(RE_2O_3)_{0.05}$ samples with RE = La, Nd, and Sm.

As shown in Figure 5, the average crystallite size in RE-substituted $Fe_{0.65}Co_{0.35}$ (3 h) samples is slightly smaller than that for the pure $Fe_{0.65}Co_{0.35}$ (3 h) alloy, except for the Sm-substituted sample. On the other hand, the microstrain values are larger in the $(Fe_{0.65}Co_{0.35})_{0.95}(RE_2O_3)_{0.05}$ samples with RE = La, Nd, and Sm than in the $Fe_{0.65}Co_{0.35}$ alloy. This behavior could be explained by the difference between the mechanical alloying process of ductile–ductile powders (Fe–Co) and ductile–fragile ones (Fe, Co-RE_2O_3). In the first stage of ductile–fragile powders milling, the ductile particles (Fe, Co) exhibited

plastic deformation, while the brittle particles (RE_2O_3) exhibited fragmentation. After the welding of the ductile particles, the fragile particles are placed between ductile particles at the collision time [32]. The fragmented particles are placed in the interfacial boundaries of the welded particles during effective high-energy ball milling. These successive phenomena, severe deformation, cold welding and solid dispersion, generate various defects (mainly dislocations) that lead to the increase in microstrain, material hardening and the enhancement of fragmentation. At the final stage, the equilibrium between the welding and fracture mechanisms is observed, leading to the formation of composite particles with a refined microstructure. In addition, the inclusions of the secondary phases at the grain boundaries inhibit the diffusion and hinder the growth of grains. The difference between Fe, Co metallic radii and *RE* covalent radii inside the lattice generates local disturbance and creates a strain in the crystal, which, in general, affects the nucleation rate and the crystallite sizes.

3.3. Mössbauer Spectrometry

The Mössbauer spectra measured at room temperature for the base sample of $Fe_{0.65}Co_{0.35}$ (0 h) and $Fe_{0.65}Co_{0.35}$ (3 h) alloy, $(Fe_{0.65}Co_{0.35})_{0.95}(RE_2O_3)_{0.05}$ samples with *RE* = La, Nd, and Sm milled for 3 h, are shown in the Figure 6, together with the calculated data.
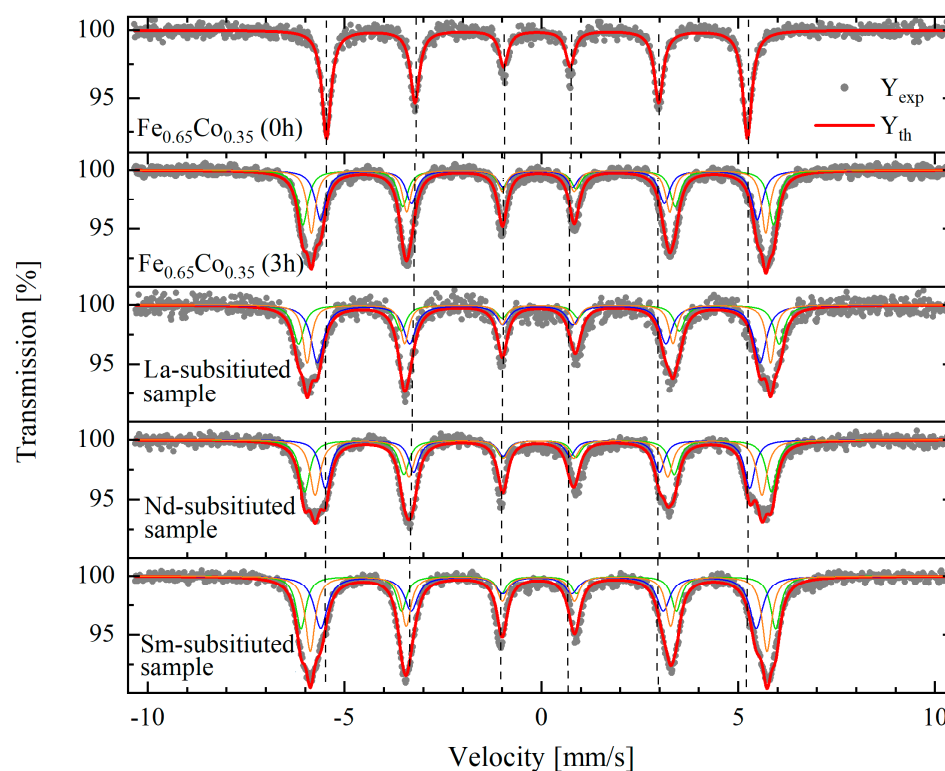

Figure 6. Mössbauer spectra of the base sample of $Fe_{0.65}Co_{0.35}$ (0 h), $Fe_{0.65}Co_{0.35}$ (3 h) alloy, and $(Fe_{0.65}Co_{0.35})_{0.95}(RE_2O_3)_{0.05}$ samples with *RE* = La, Nd, and Sm milled for 3 h. Full circles - measured data; blue, orange and green - three fit components; red - resulting fit.

For the raw sample (mixture of initial powders), one sextet component was sufficient to satisfactorily fit the experimental data. The spectra for the $Fe_{0.65}Co_{0.35}$ alloy and composites with RE_2O_3 were fitted with three magnetically split (sextet) components. Hyperfine interaction parameters (isomer shift and hyperfine magnetic field) for each component (denoted as S1, S2, and S3), together with its relative contribution, are listed in the Table 2. In addition, the mean value of the hyperfine magnetic field, <*H*> and the isomer shift, with respect to *α*-Fe calibration <*IS*> for each sample, are presented in Table 2.

Table 2. Hyperfine interactions parameters for each sextet (*S*) (relative contribution and isomer shift with respect to Fe – *IS*; hyperfine magnetic field – *H*) for each component and their respective mean values (*<IS>*, *<H>*) obtained from the fits of measured Mössbauer spectra.

Samples	S	Rel. Contrib. [%]	*IS* Fe [mm/s]	*H* [T]	*<IS>* [mm/s]	*<H>* [T]
$Fe_{0.65}Co_{0.35}$ (0 h)	S1	100	0.002(1)	33.3(5)	—	—
$Fe_{0.65}Co_{0.35}$ (3 h)	S1	34.0	0.045(2)	37.0(4)	0.041	35.7
	S2	33.3	0.039(2)	34.3(4)		
	S3	32.7	0.039(3)	35.7(3)		
La-substituted sample	S1	25.7	0.068(7)	37.8(9)	0.048	36.1
	S2	44.3	0.034(5)	34.8(7)		
	S3	30.0	0.051(4)	36.4(5)		
Nd-substituted sample	S1	33.9	0.043(4)	36.7(5)	0.031	35.2
	S2	31.0	0.005(4)	33.4(4)		
	S3	35.1	0.040(4)	35.1(5)		
Sm-substituted sample	S1	27.2	0.045(3)	37.3(5)	0.037	35.7
	S2	35.6	0.025(4)	34.2(6)		
	S3	37.2	0.042(2)	35.9(3)		

The Mössbauer spectrum of the raw $Fe_{0.65}Co_{0.35}$ (0 h) shows a sextet typical for magnetic behavior with a mean hyperfine magnetic field *<H>* ~ 33.0 T and an average isomer shift *<IS>* = 0.0021(10) mm/s. This behavior corresponds to the pure bcc-Fe, i.e., Fe has only Fe atoms in the neighbor's shells, as no cobalt substitution takes place. This result shows that for a raw sample there is no Fe–Co interaction. After 3 h of milling, a broadening of the external lines is observed in the $Fe_{0.65}Co_{0.35}$ (3 h) Mössbauer spectra. This effect is attributed to the substitution of the Fe atoms by Co atoms in Fe–Co systems. The increase in the average hyperfine magnetic field to 35.7 T and the disappearance of the component with a magnetic field of 33.3 T is due to the formation of the $Fe_{0.65}Co_{0.35}$ (3 h) alloy, where Fe atoms coexist with randomly distributed Co atoms occupying bcc-Fe sites. This is further confirmed by an increase in the isomer shift up to 0.04 mm/s. These values are similar to those reported in previous works for the Fe–Co alloys [14,33].

The spectra of *RE*-substituted $Fe_{0.65}Co_{0.35}$ (3 h) samples show three sextets, indicating the coexistence of different magnetic environments of Fe atoms. The La-substituted $Fe_{0.65}Co_{0.35}$ (3 h) presents the highest average hyperfine field (36.1 T), which is in close agreement with the values found by Zelenakova et al. (36.16 T) [34]. For Nd- and Sm-substituted compositions, the average hyperfine field is about 35.0 T, which is in agreement with previous works for Fe–Co milled alloys [33,35,36]. The presence of *RE* elements in the Fe–Co structure may generate additional sextets in the Mössbauer spectra. The magnetic patterns were detected in the Mössbauer spectra of the *RE*-substituted $Fe_{0.65}Co_{0.35}$ (3 h) due to a small *RE* concentration.

3.4. The Magnetic Properties

The effect of RE_2O_3 (*RE* = La, Nd, and Sm) addition on the magnetic properties of $Fe_{0.65}Co_{0.35}$ (3 h) nanoparticles was investigated, based on the *M* vs. *H* dependencies, recorded at 10 K and 300 K. Figure 7 presents the hysteresis loops for the $Fe_{0.65}Co_{0.35}$ (3 h) alloy and $(Fe_{0.65}Co_{0.35})_{0.95}(RE_2O_3)_{0.05}$ samples with *RE* = La, Nd, and Sm showing soft ferromagnetic behavior.
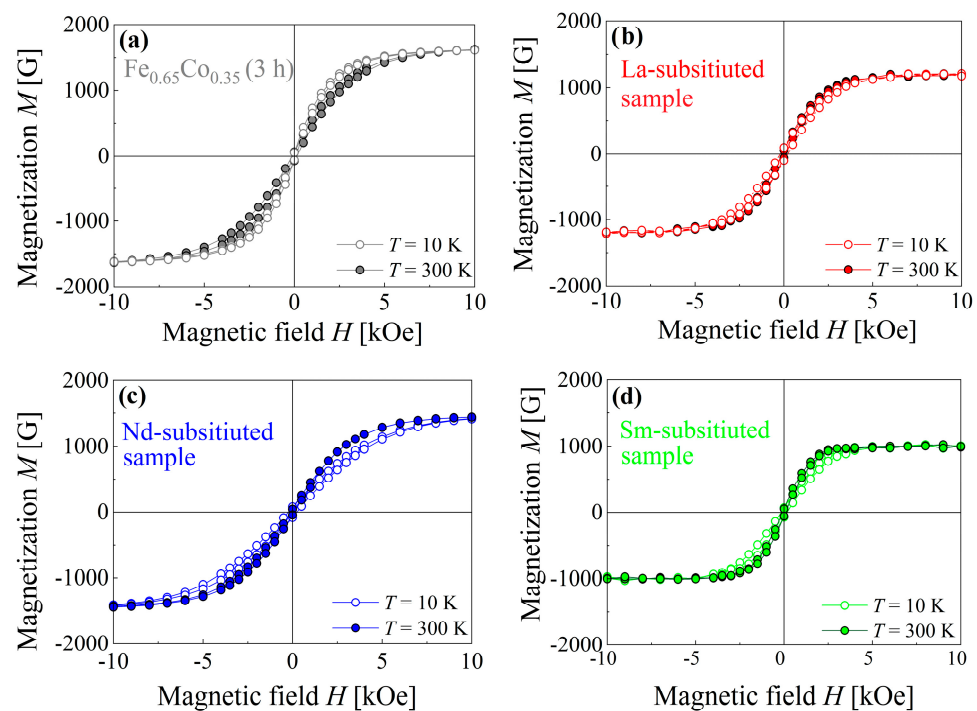
Figure 7. Magnetization *M* as a function of the magnetic field *H* for (**a**) $Fe_{0.65}Co_{0.35}$ (3 h) alloy and $(Fe_{0.65}Co_{0.35})_{0.95}(RE_2O_3)_{0.05}$ samples with *RE* = (**b**) La, (**c**) Nd, and (**d**) Sm, recorded at 10 K and 300 K.

Table 3 summarizes the magnetic properties of saturation magnetization (M_s), coercive field (H_c), remnant magnetization (M_r) and magnetic energy product (E_M) derived from these hysteresis loops for all investigated compositions.

Table 3. The magnetic properties of *RE*-substituted $Fe_{0.65}Co_{0.35}$ (3 h).

Compound	M_s [G]		M_r [G]		H_c [Oe]		E_M [MG·Oe]	
	10 [K]	300 [K]	10 [K]	300 [K]	10 [K]	300 [K]	10 [K]	300 [K]
$Fe_{0.65}Co_{0.35}$ (3 h)	1690(10)	1660(10)	67(7)	57(7)	130(2)	75(5)	1.414	0.649
La-substituted sample	1205(15)	1190(10)	97(7)	56(6)	290(5)	100(5)	0.630	0.450
Nd-substituted sample	1515(15)	1490(10)	78(8)	42(5)	260(5)	100(10)	3.312	0.608
Sm-substituted sample	1025(10)	1000(10)	68(8)	52(5)	330(5)	85(5)	1.688	0.710

For *T* = 300 K, the saturation magnetization value of $Fe_{0.65}Co_{0.35}$ (3 h) equals 1660(10) G, whereas the saturation magnetization values of the *RE*-substituted $Fe_{0.65}Co_{0.35}$ nanoparticles with La^{3+}, Nd^{3+}, and Sm^{3+} are equal to 1190(10) G, 1490(10) G, and 1000(10) G, respectively. The saturation magnetization value of the *RE*-substituted $Fe_{0.65}Co_{0.35}$ (3 h) nanoparticles decreased by 40% when compared with the pure one. The magnetic exchange interactions play a key role in the magnetization process in the nanoparticles. The *RE* (La^{3+}, Nd^{3+}, and Sm^{3+}) ions partially replace Fe atoms. The ionic radii of La^{3+}, Nd^{3+}, and Sm^{3+} ions are higher than the atomic radii of Fe atoms, which results in the weakening of the exchange interactions. This causes a decrease in M_s for the substituted compounds; thus, the saturation magnetization of the $Fe_{0.65}Co_{0.35}$ (3 h) system is reduced [37,38].

The decrease in M_s for *RE*-substituted samples is caused by the decrease in the Fe–Fe and Fe–Co interactions (3*d*–3*d* coupling), due to the reduction in the concentration of Fe and Co ferromagnetic atoms, together with the presence of very weak *RE*–Fe (4*f*–3*d* coupling) and *RE*–*RE* (4*f*–4*f* coupling) interactions, when compared to 3*d*–3*d* ones [39,40]. The saturation magnetization value of *RE*-substituted $Fe_{0.65}Co_{0.35}$ nanoparticles depends

mainly on their magnetic moments. The M_s value for Nd-substituted $Fe_{0.65}Co_{0.35}$ (3 h) nanoparticles is higher than for the other samples. This is explained by the fact that the Nd^{3+} ions have a higher magnetic moment ($J = 3.6\mu_B$), when compared with La^{3+} and Sm^{3+} ions ($J = 0$ and $J = 1.38\mu_B$) [41]. The coercivity values of RE-substituted $Fe_{0.65}Co_{0.35}$ (3 h) nanoparticles are higher than those for the pure $Fe_{0.65}Co_{0.35}$ nanoparticles. It is well known that the coercivity is strongly influenced by the microstructure and heavy plastic deformation during the MA process, which leads to the formation of defects and generation of internal strain inside the material [42,43].

The maximum coercivity values were reported for the La-, Nd-substituted $Fe_{0.65}Co_{0.35}$ (3 h) samples. As pointed out by XRD characterization, the solubility of La^{3+} and Nd^{3+} ions in the $Fe_{0.65}Co_{0.35}$ (3 h) structure is limited and some ions do not enter the Fe lattice structure, but precipitate as secondary phases at the grain boundaries. The antiferromagnetic behavior of these secondary phases significantly alters the magnetic response of the samples. Moreover, the presence of inclusions hinders the domain walls' motion. As a result, the coercive field of the La- and Nd-substituted samples is higher (100(5) Oe for the La-substituted sample and 100(10) Oe for the Nd-substituted, respectively) than for other samples (85(5) Oe for the Sm-substituted sample and 75(5) Oe for the $Fe_{0.65}Co_{0.35}$ (3 h) alloy). However, for the La-substituted material, the magnetic energy product (E_M) is the smallest (at 300 K), and is equal to 0.450 MG·Oe.

For $T = 10$ K, an enhancement of both M_s and H_c values of all prepared nanoparticles was noticed. The highest M_s value of 1515(15) G was observed for the Nd-substituted sample, which was ~2% higher than that observed at 300 K. In the La-substituted sample, we observed a lower value of saturation magnetization. The Sm-substituted nanoparticles demonstrate the lowest value of M_s, 1025(10) G. The magnetization is mainly governed by the spin state and the magnetic moments of atoms; thus, the increase in M_s was principally due to the reduction in thermal fluctuation of the magnetic moments, and therefore the increase in magnetic ordering [44–47]. The coercivity has shown a substantial increase at 10 K, for all the investigated nanoparticles. For La- and Nd-substituted samples, the increase in H_c ranged from 100(5) Oe for 300 K to 290 K and 260(5) Oe for 10 K (by ~66% and ~62%, respectively). We noted a higher value for the Sm-substituted sample with an increase from 85(5) Oe for 300 K to 330(5) Oe for 10 K (by ~75%). It is apparent that H_c is strongly dependent on temperature. For a particle, thermal energy is essential to reverse its spin and to overcome the energy barrier. For $T = 10$ K, the particles did not have sufficient thermal energy; therefore, they required a stronger field to reverse the magnetization [48].

3.5. Differential Scanning Calorimetry (DSC) Analysis

The structural stability was studied using the differential scanning calorimetry (DSC) method. Figure 8a presents the DSC curves of the $Fe_{0.65}Co_{0.35}$ (3 h) alloy, and $(Fe_{0.65}Co_{0.35})_{0.95}(RE_2O_3)_{0.05}$ samples with RE = La, Nd, and Sm, mechanically alloyed for 3 h in the mechanosynthesis process during effective high-energy ball milling. The results confirm the formation of solid solutions.

A broad exothermic peak occurs at the temperature range 110 – 120 °C for all investigated compounds. This peak originates from the recovery, strain relaxation, grain growth and recrystallization of the nanocrystalline compositions [48]. The DSC scans show the presence of two main exothermic peaks. The first one is broad with the onset temperature of 670–680 °C, which can be attributed to the disordered (bcc) – ordered B2 (bcc) structural transformation. This is in good agreement with the Fe–Co phase diagram [49,50]. The second sharp peak observed for all investigated samples is related to the transition from body-centered cubic ferromagnetic to the face-centered cubic paramagnetic structure [50].

Note that the onset temperatures of the peaks are 987 °C, 994.8 °C, 995.6 °C, and 996.4 °C for $Fe_{0.65}Co_{0.35}$ (3 h) alloy, Sm-substituted sample – $(Fe_{0.65}Co_{0.35})_{0.95}(Sm_2O_3)_{0.05}$, Nd-substituted sample – $(Fe_{0.65}Co_{0.35})_{0.95}(Nd_2O_3)_{0.05}$, and La-substituted sample – $(Fe_{0.65}Co_{0.35})_{0.95}(La_2O_3)_{0.05}$, respectively (Figure 8b). It seems that the RE_2O_3 addition stabilizes the bcc structure at high temperatures and increases the magnetic order temperature of the $Fe_{0.65}Co_{0.35}$ alloy.
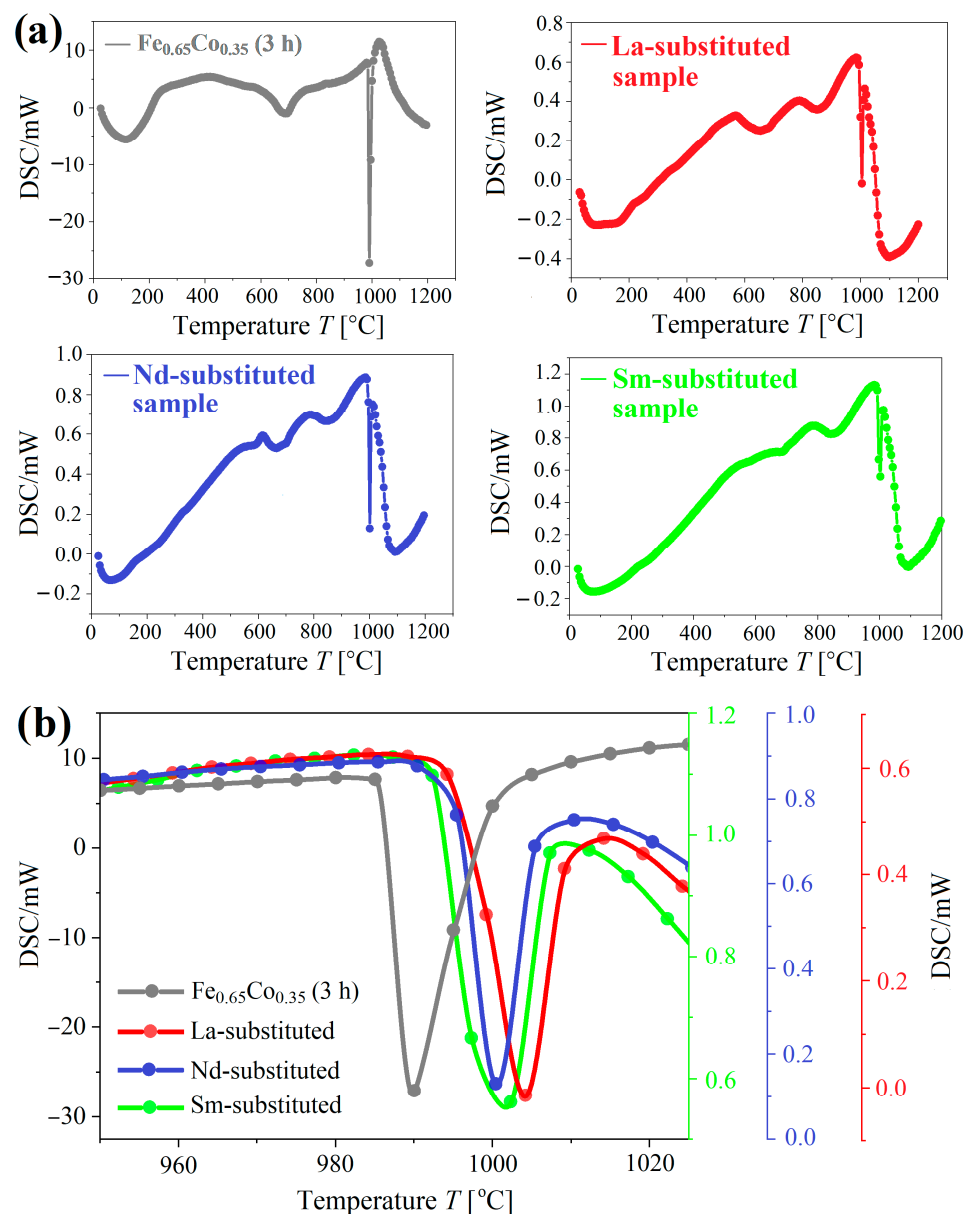
Figure 8. (**a**) The DSC curves for $Fe_{0.65}Co_{0.35}$ (3 h) alloy, and $(Fe_{0.65}Co_{0.35})_{0.95}(RE_2O_3)_{0.05}$ samples with RE = La, Nd, and Sm, mechanically alloyed for 3 h in the mechanosynthesis process during effective high-energy ball milling. (**b**) The sharp peaks in all alloys related to the transition from body-centered cubic (bcc) ferromagnetic to the face-centered cubic (fcc) paramagnetic structure (range 950 – 1040 °C).

4. Conclusions

The pure $Fe_{0.65}Co_{0.35}$ (3 h) alloy and $(Fe_{0.65}Co_{0.35})_{0.95}(RE_2O_3)_{0.05}$ samples with RE = La, Nd, and Sm SMNs were successfully prepared with the mechanical alloying method. The research reported particles (agglomerates) of irregular shape that were 0.2–12 μm in size. According to EDS analysis, uniform distribution of the elements was achieved. The homogeneous phase formation in the investigated samples was confirmed using the XRD technique.

The X-ray diffraction patterns of the substituted $Fe_{0.65}Co_{0.35}$ (3 h) alloy demonstrated the bcc-Fe structure with traces of Fe_3O_4 that originated from the initial impurity of the Fe powder used. Rietveld refinement was used to obtain the lattice parameter, crystallite size and microstrain values. The RE-substituted $Fe_{0.65}Co_{0.35}$ nanoparticles showed a similar

crystallite size (30–50 nm) and higher microstrain, when compared to the pure $Fe_{0.65}Co_{0.35}$ (3 h). The La-substituted sample seemed to behave differently from the other samples, presumably due to the larger La radius, compared to the other rare-earth metals. This was reflected in the hyperfine interactions, as it exhibited the largest mean isomeric shift and hyperfine magnetic field values (larger than for the parent alloy).

Magnetic measurements performed at 10 K and 300 K have shown the soft ferromagnetic nature of the $(Fe_{0.65}Co_{0.35})_{0.95}(RE_2O_3)_{0.05}$ nanocomposites. The magnetization saturation and coercivity were found to be strongly dependent on *RE*-substitution and temperature. *RE*-substitution increased the magnitude of H_c and decreased the M_s. At 300 K, the La-substituted sample was softer (0.450 MG·Oe) than the parent alloy (0.608 MG·Oe), requiring lower energy to reverse magnetization. On the other hand, for the Sm-substituted sample, higher energy was required to flip magnetization (0.710 MG·Oe). Substitution stabilizes the bcc structure at high temperatures, which is associated with an increase in the magnetic ordering temperature of the $(Fe_{0.65}Co_{0.35})_{0.95}(RE_2O_3)_{0.05}$ samples, with respect to the parent alloy. For La-substituted sample, the highest ordering temperature of 1006 °C was reported. Low temperature behavior is also strongly modified by substitution with rare-earth metals. The coercive field increases at least by a factor of 2, while the remanence only slightly increases. The reported research shows a simple and effective route to produce novel materials with desired magnetic properties.

References

1. Hasegawa, T.; Kanatani, S.; Kazaana, M.; Takahashi, K.; Kumagai, K.; Hirao, M.; Ishio, S. Conversion of FeCo from soft to hard magnetic material by lattice engineering and nanopatterning. *Sci. Rep.* **2017**, *7*, 13215. [CrossRef] [PubMed]
2. Alonso, J.; Khurshid, H.; Sankar, V.; Nemati, Z.; Phan, M.H.; Garayo, E.; García, J.A.; Srikanth, H. FeCo nanowires with enhanced heating powers and controllable dimensions for magnetic hyperthermia. *J. Appl. Phys.* **2015**, *117*, 17D113. [CrossRef]
3. Habib, A.H.; Ondeck, C.L.; Chaudhary, P.; Bockstaller, M.R.; McHenry, M.E. Evaluation of iron-cobalt/ferrite core-shell nanoparticles for cancer thermotherapy. *J. Appl. Phys.* **2008**, *103*, 2012–2015. [CrossRef]
4. Lee, J.L.; Sherlock, S.P.; Terashima, M.; Kosuge, H.; Suzuki, Y.; Goodwin, A.P.; Robinson, J.; Seo, W.S.; Liu, Z.; Loung, R.; et al. High-contrast in vivo visualization of microvessels using novel FeCo/GC magnetic nanocrystals. *Mag. Res. Med.* **2009**, *62*, 1497–1509. [CrossRef] [PubMed]
5. Seo, W.S.; Lee, J.H.; Sun, X.; Suzuki, Y.; Mann, D.; Liu, Z.; Terashima, M.; Yang, P.C.; McConnell, M.V.; Nishimura, D.G.; et al. FeCo/graphitic-shell nanocrystals as advanced magnetic-resonance-imaging and near-infrared agents. *Nat. Mater.* **2006**, *5*, 971–976. [CrossRef] [PubMed]

6. Wen, X.; Jackson, E.F.; Price, R.E.; Kim, E.E.; Wu, Q.; Wallace, S.; Charnsangavej, C.; Gelovani, J.G.; Li, C. Synthesis and characterization of poly(L-glutamic acid) gadolinium chelate: A new biodegradable MRI contrast agent. *Bioconjug. Chem.* **2004**, *15*, 1408–1415. [CrossRef] [PubMed]

7. Das, B.K.; Rastogi, A.C. Thin films for secondary data storage. *IETE J. Res.* **1997**, *43*, 221–232. [CrossRef]

8. Zare, Y.; Shams, M.H.; Jazirehpour, M. Tuning microwave permittivity coefficients for enhancing electromagnetic wave absorption properties of FeCo alloy particles by means of sodium stearate surfactant. *J. Alloys Compd.* **2017**, *717*, 294–302. [CrossRef]

9. Chrobak, A. High and ultra-high coercive materials in spring-exchange systems—Review, simulations and perspective. *Materials* **2022**, *15*, 6506. [CrossRef]

10. Berasategi, J.; Gomez, A.; Bou-Ali, M.M.; Gutiérrez, J.; Barandiarán, J.M.; Beketov, I.V.; Safronov, A.P.; Kurlyandskaya, G.V. Fe nanoparticles produced by electric explosion of wire for new generation of magneto-rheological fluids. *Smart Mater. Struct.* **2018**, *27*, 045011. [CrossRef]

11. Hou, C.; Shan, Y.; Wu, H.; Bi, X. Effect of a small addition of Cr on soft magnetic and mechanical properties of Fe-49Co-2V alloy. *J. Alloys Compd.* **2013**, *556*, 51–55. [CrossRef]

12. Khosravi, S.; Alizadeh, M.; Sharafi, S.; Karimi-Maleh, H.; Atar, N. Structural, magnetic and electron transfer effect of Cr additive on $Fe_{65}Co_{35}$ nanopowder fabricated mechanical alloying. *Powder Technol.* **2015**, *279*, 262–268. [CrossRef]

13. Hocine, M.; Guittoum, A.; Hemmous, M.; Martínez-Blanco, D.; Gorria, P.; Rahal, B.; Blanco, J.A.; Sunol, J.J.; Laggoun, A. The role of silicon on the microstructure and magnetic behaviour of nanostructured $(Fe_{0.7}Co_{0.3})_{100-x}Si_x$ powders. *J. Magn. Magn. Mater.* **2017**, *422*, 149–156. [CrossRef]

14. Yousefi, M.; Sharafi, S. The effect of simultaneous addition of Si and Co on microstructure and magnetic properties of nanostructured iron prepared by mechanical alloying. *Mat. Design* **2012**, *37*, 325–333. [CrossRef]

15. Chaudhary, V.; Ping Tan, L.; Sharma, V.K.; Ramanujan, R.V. Accelerated study of magnetic Fe–Co–Ni alloys through compositionally graded spark plasma sintered samples. *J. Alloys Compd.* **2021**, *869*, 159318. [CrossRef]

16. Jain, V.; Chandra, A.R.; Lakshmi, N.; Reddy, V.R.; Jani, S. Magnetic behaviour of ^{57}Fe/Co/Al multilayers deposited on a glass substrate. *Bull. Mater. Sci.* **2019**, *42*, 161. [CrossRef]

17. Sarkar, A.; Hembram, S.; Chatterjee, S.; Basu Mallick, A. Effect of annealing treatments on the magnetic properties of FeCo/Cu core shell nanostructures. *Mater. Today Proc.* **2018**, *5*, 745–751. [CrossRef]

18. Vadillo, V.; Gutiérrez, J.; Insausti, M.; Garitaonandia, J.S.; de Muro, I.G.; Quintana, I.; Barandiaran, J.M. Synthesis and characterization of Fe-Co-V high magnetization nanoparticles obtained by physical routes. *IEEE Magn. Lett.* **2019**, *10*, 6104805. [CrossRef]

19. Xu, F.; Xu, Z.; Yin, Y. Tuning of the microwave magnetization dynamics in Dy-doped $Fe_{65}Co_{35}$-based thin films. *IEEE Trans. Magn.* **2015**, *51*, 2800904. [CrossRef]

20. Younsi, K.; Russier, V.; Bessais, L. Structure and magnetic properties of nanocrystalline $PrCo_3$. *J. Appl. Phys.* **2010**, *107*, 083916. [CrossRef]

21. Younsi, K.; Crivello, J.C.; Paul-Boncour, V.; Bessais, L.; Porcher, F.; André, G. Study of the magnetic and electronic properties of nanocrystalline $PrCo_3$ by neutron powder diffraction and density functional theory. *J. Phys. Condens. Matter.* **2013**, *25*, 116001. [CrossRef] [PubMed]

22. Sirvent, P.; Berganza, E.; Aragón, A.M.; Bollero, A.; Moure Arroyo, A.; García-Hernández, M.; Marín, P.; Fernández, J.; Quesada, A. Effective high-energy ball milling in air of Fe65Co35 alloys. *J. Alloys Compd.* **2014**, *115*, 17B505. [CrossRef]

23. Chermahini, M.D.; Zandrahimi, M.; Shokrollahi, H.; Sharafi, S. The effect of milling time and composition on microstructural and magnetic properties of nanostructured Fe-Co alloys. *J. Alloys Compd.* **2009**, *477*, 45–50. [CrossRef]

24. Manh, D.H.; Tung, D.K.; Phong, L.T.H.; Phuc, N.X.; Jutimoosik, J.; Yimnirun, R. Complementary studies of phase formation during fabrication of $Fe_{0.65}Co_{0.35}$ nanoparticles by mechanical alloying. *J. Elec. Mat.* **2016**, *45*, 2501–2507.

25. Hosseini, H.R.M.; Bahrami, A. Preparation of nanocrystalline Fe-Si-Ni soft magnetic powders by mechanical alloying. *Mater. Sci. Eng. B Sol. Stat. Mater. Adv. Technol.* **2005**, *123*, 74–79. [CrossRef]

26. Gadkari, A.; Shinde, T.; Vasambekar, P. Influence of rare-earth ions on structural and magnetic properties of $CdFe_2O_4$ ferrites. *Rare Met.* **2010**, *29*, 168–173. [CrossRef]

27. Suo, N.; Sun, A.; Yu, L.; Zuo, Z.; Pan, X.; Zhang, W.; Zhao, X.; Zhang, Y.; Shao, L. Effect of different rare earth (RE = Y^{3+}, Sm^{3+}, La^{3+}, and Yb^{3+}) ions doped on the magnetic properties of Ni–Cu–Co ferrite nanomagnetic materials. *J. Mater. Sci. Mater. Electron.* **2021**, *32*, 246–264. [CrossRef]

28. Kanna, R.R.; Sakthipandi, K.; Seeni Mohamed Aliar Maraikkayar, S.M.; Lenin, N.; Sivabharathy, M. Doping effect of rare-earth (lanthanum, neodymium and gadolinium) ions on structural, optical, dielectric and magnetic properties of copper nanoferrites. *J. Rare Earths* **2018**, *36*, 1299–1309. [CrossRef]

29. Shannon, R.D.; Prewitt, C.T. Effective ionic radii in oxides and fluorides. *Acta Crystallogr. B* **1969**, *25*, 925–945. [CrossRef]

30. Chaubey, G.S.; Barcena, C.; Poudyal, N.; Rong, C.; Gao, J.; Sun, S.; Liu, J.P. Synthesis and stabilization of FeCo nanoparticles. *J. Am. Chem. Soc.* **2007**, *129*, 7214–7215. [CrossRef] [PubMed]

31. Klencsár, Z.; Németh, P.; Sándor, Z.; Horváth, T.; Sajó, I.E.; Mészáros, S.; Mantilla, J.; Coaquira, J.A.H.; Garg, V.K.; Kuzmann, E.; et al. Structure and magnetism of Fe-Co alloy nanoparticles. *J. Alloys Comp.* **2016**, *674*, 153–161. [CrossRef]

32. Zhang, X.; Yan, Q.; Yang, C.; Wang, T.; Ge, C. Microstructure, mechanical properties and bonding characteristic of deformed tungsten. *Int. J. Refract. Met. Hard Mater.* **2014**, *43*, 302–308. [CrossRef]

33. Moumeni, H.; Alleg, S.; Djebbari, C.; Bentayeb, F.Z.; Grenèche, J.M. Synthesis and characterisation of nanostructured FeCo alloys. *J. Mater. Sci.* **2004**, *39*, 5441–5443. [CrossRef]

34. Zeleňáková, A.; Olekšáková, D.; Degmová, J.; Kováč, J.; Kollár, P.; Kusý, M.; Sovák, P. Structural and magnetic properties of mechanically alloyed FeCo powders. *J. Magn. Magn. Mater.* **2007**, *316*, e519–e522. [CrossRef]

35. Moumeni, H.; Alleg, S.; Greneche, J.M. Structural properties of Fe50Co50 nanostructured powder prepared by mechanical alloying. *J. Alloys Compd.* **2005**, *386*, 12–19. [CrossRef]

36. Rincón Soler, A.I.; Rodríguez Jacobo, R.R.; Medina Barreto, M.H.; Cruz-Muñoz, B. Structural and magnetic properties of FeCoC system obtained by mechanical alloying. *Hyperfine Interact.* **2017**, *238*, 48. [CrossRef]

37. Majeed, A.; Khan, M.A.; Raheem, F.; Hussain, A.; Iqbal, F.; Murtaza, G.; Akhtar, M.N.; Shakir, I.; Warsi, M.F. Structural elucidation and magnetic behavior evaluation of rare earth (La, Nd, Gd, Tb, Dy)-doped BaCoNi–X hexagonal nano-sized ferrites. *J. Magn. Magn. Mater.* **2016**, *408*, 147–151. [CrossRef]

38. Kanna, R.R.; Lenin, N.; Sakthipandi, K.; Kumar, A.S. Structural, optical, dielectric, and magnetic studies of gadolinium-added Mn-Cu nanoferrites. *J. Magn. Magn. Mater.* **2018**, *453*, 78–90. [CrossRef]

39. Padalia, D.; Johri, U.C.; Zaidi, M.G.H. Effect of cerium substitution on structural and magnetic properties of magnetite nanoparticles. *Mater. Chem. Phys.* **2016**, *169*, 89–95. [CrossRef]

40. Prozorov, T.; Bazylinski, D.A.; Mallapragada, S.K. Novel magnetic nanomaterials inspired by magnetotactic bacteria: Topical review. *Mat. Sci. Eng.* **2013**, *R.74*, 133–172. [CrossRef]

41. Dalal, M. *A Textbook of Physical Chemistry*, 1st ed.; Dalal Institute: Rohtak, India, 2017; Volume 1.

42. Lu, G.D.; Miao, X.S.; Cheng, W.M.; Huang, X.F.; Yang, L.; Pan, L.Q. Influence of Cu underlayer on the high-frequency magnetic properties of FeCoSiO thin films. *IEEE Trans. Magn.* **2015**, *51*, 2801504. [CrossRef]

43. Yang, B.; Wu, Y.; Li, X.; Yu, R. Chemical synthesis of high-stable amorphous FeCo nanoalloys with good magnetic properties. *Nanomaterials* **2018**, *8*, 154. [CrossRef] [PubMed]

44. Almessiere, M.A.; Slimani, Y.; Baykal, A. Structural and magnetic properties of Ce-doped strontium hexaferrite. *Ceram. Int.* **2018**, *44*, 9000–9008. [CrossRef]

45. Almessiere, M.A.; Slimani, Y.; Sertkol, M.; Gungunes, H.; Wudil, Y.S.; Demir Korkmaz, A.; Baykal, A. Impact of Gd substitution on the structure, hyperfine interactions, and magnetic properties of Sr hexaferrites. *Ceram. Int.* **2021**, *47*, 33853–33864. [CrossRef]

46. Slimani, Y.; Güngüneş, H.; Nawaz, M.; Manikandan, A.; El Sayed, H.S.; Almessiere, M.A.; Sözeri, H.; Shirsath, S.E.; Ercan, I.; Baykal, A. Magneto-optical and microstructural properties of spinel cubic copper ferrites with Li–Al co-substitution. *Ceram. Int.* **2018**, *44*, 14242–14250. [CrossRef]

47. Kumar, D.; Sarin, A.; Verma, V.; Venkatraman, R. Pulsed laser deposition assisted fabrication and characterization of Fe-Co nanoparticles embedded in TiN thin film matrix. *Thin Solid Film.* **2013**, *534*, 561–565. [CrossRef]

48. Poudyal, N.; Rong, C.; Zhang, Y.; Wang, D.; Kramer, M.J.; Hebert, R.J.; Ping Liu, J. Self-nanoscaling in FeCo alloys prepared via severe plastic deformation. *J. Alloys Compd.* **2012**, *521*, 55–59. [CrossRef]

49. Chitsazan, B.; Shokrollahi, H.; Behvandi, A.; Mirzaee, O. Characterization and magnetic coercivity of nanostructured $(Fe_{50}Co_{50})_{100-X}V_{X=0,2,4}$ powders containing a small amount of Co 3V intermetallic obtained by mechanical alloying. *Powder Technol.* **2011**, *214*, 105–110. [CrossRef]

50. Sourmail, T. Near equiatomic FeCo alloys: Constitution, mechanical and magnetic properties. *Prog. Mater. Sci.* **2005**, *50*, 816–880. [CrossRef]